https://doi.org/10.5194/egusphere-2026-3754
Preprint. Discussion started: 2 July 2026


# Influence of model spatial resolution on Sargassum beaching predictions along the Mexican Caribbean coast

Ana Lucia de Santos Medina[1], Sheila Natali Estrada Allis[1], Lorena Guerrero Moreno[1], Paulina Cetina Heredia[1]

[1]Department of Physical Oceanography, Centre for Scientific Research and Higher Education of Ensenada, Baja California, 22860, Mexico

*Correspondence to*: Ana Lucia de Santos Medina (luciadesanmed@gmail.com)

**Abstract.** The sensitivity of Sargassum transport predictions to ocean circulation model resolution remains poorly quantified in the Mexican Caribbean, despite its relevance for operational forecasting systems. Here, we assess how horizontal resolution (5 km vs. 1 km) of simulations with the Regional Ocean Modeling System (ROMS) modulates Lagrangian particle trajectories and subsequent coastal landings. Four 10-day forecast case studies, including forcing conditions for different atmospheric and ocean dynamics, were analysed using particle tracking and finite-time Lyapunov exponent (FTLE) diagnostics to evaluate the effect of current spatial resolution on particle distribution and dispersion. Results reveal that resolution-dependent differences in landing percentages are strongly dependent upon the predominant circulation regime. Under typical conditions and circulation field, both resolutions produce comparable large-scale transport pathways and similar regional landing patterns. In contrast, under extreme event conditions (i.e., tropical cyclone), the 1-km simulation resolves wind-driven submesoscale structures that disrupt dominant advective transport, leading to substantial shifts in coastal accumulation patterns. The most significant differences in particles' landings occurred in regions of complex coastal geometry, where shoreline curvature and island systems enhance sensitivity to small-scale circulation features. Despite these differences, both model resolutions identified recurrent accumulation hotspots near the Sian Ka'an Reserve, Banco Chinchorro, and Cozumel. These findings suggest that ocean circulation models with a 5 km spatial resolution are adequate for short-term regional forecasting of Sargassum beach landings, but higher-resolution simulations become critical under extreme events and in morphologically complex coastal environments in the Mexican Caribbean. More broadly, this study highlights the state-dependent nature of resolution requirements in Lagrangian coastal transport modelling and provides guidance for balancing computational cost and predictive skill in operational Sargassum forecast systems.

## 1 Introduction

Sargassum is a genus of brown macroalgae that includes two pelagic species: *Sargassum natans* and *Sargassum fluitans*. These species form floating rafts that serve as habitats for a wide variety of marine organisms (Lapointe, 1986; Lapointe et al., 2014; Moser and Lee, 2012; Rooker et al., 2006; Witherington et al., 2012). However, large Sargassum accumulations that reach coastal areas pose serious ecological, economic, and public health challenges (Chavez et al., 2020; Hu et al., 2016; Rodriguez-

https://doi.org/10.5194/egusphere-2026-3754
Preprint. Discussion started: 2 July 2026


Martinez et al., 2019; Rodriguez-Muñoz et al., 2021; van Tussenbroek et al., 2017). Large accumulations of Sargassum have been observed in the tropical Atlantic since 2011 (Wang et al., 2019). The first major influx into the Caribbean Sea was reported in 2014, with similar events recurring in subsequent years (Cuevas et al., 2018; Maurer et al., 2015; Schell et al., 2015; Wang et al., 2019); some of these fluxes have culminated in major Sargassum strandings that significantly affected the Mexican Caribbean coast (Jouanno et al., 2025; Lara-Hernandez et al., 2024; Rodriguez-Martinez et al., 2022; van Tussenbroek et al., 2017). In response, two mitigation strategies have been implemented: beach collection and open-sea harvesting (Chavez et al., 2020). However, if not carefully managed, these approaches can fail or lead to ecological and environmental impacts (Chavez er al., 2020). Therefore, forecasting systems capable of predicting the timing and location of beaching events accurately are essential to optimize collection efforts while minimizing environmental disturbance.

The size, distribution, and transport of Sargassum rafts are influenced by both biological growth processes and oceanic and atmospheric dynamics (Brooks et al., 2018; Marsh et al., 2021; Putman, et al, 2020; Skliris et al., 2022; Uribe-Martinez et al., 2022). Consequently, one of the main challenges in modelling Sargassum transport lies in representing both physical and biogeochemical processes operating across multiple spatial and temporal scales. Physical phenomena acting at different spatial scales can exert distinct controls on Sargassum transport and beaching. For example, transport in the tropical Atlantic may be dominated by mesoscale current advection, whereas beaching processes are more strongly influenced by smaller-scale coastal dynamics (Bourg et al., 2022; Marsh et al., 2022).

Mesoscale eddies have been shown to modulate Sargassum accumulation and redistribution across the tropical Atlantic, acting as retention or aggregation structures that influence downstream transport toward the Caribbean Sea (Andrade-Canto et al., 2022; Beron-Vera et al., 2022; Brooks et al., 2019; Sosa-Gutierrez et al., 2025). Submesoscale features (O (1-10 km)) influence biological processes indirectly, by inducing vertical velocities that affect nutrient transport, and modulating the distribution of planktonic species through horizontal dispersion (Lévy et al., 2012). For example, Zhong and Bracco (2013) investigated the effects of submesoscale processes on the transport of Lagrangian particles advected by ocean currents at spatial resolutions of 5 km and 1 km in the northwestern Gulf of Mexico. They showed that the number of submesoscale eddies and vorticity filaments increased with higher horizontal resolution and that vertical velocities increased as a result of the emergence of these submesoscale features. Additionally, their results indicated that, in a 1-km model, particle distributions were influenced by the formation of convergence zones associated with ageostrophic motions. These findings suggest that model resolution can substantially influence simulated transport pathways and accumulation patterns, with important implications for Sargassum transport and beaching predictions.

In addition to ocean circulation, wind forcing plays a critical role in Sargassum transport and beaching. Previous studies have shown that including wind effects significantly improves the accuracy of Sargassum trajectory simulations (Berline et al., 2020; Johns et al., 2020; Johnson et al., 2020; Lara-Hernandez et al., 2024; Marsh et al., 2021; Putman et al., 2018, 2020,

https://doi.org/10.5194/egusphere-2026-3754
Preprint. Discussion started: 2 July 2026


2023). Moreover, modelling results indicate that wind forcing exerts the strongest control on Sargassum landings along the Mexican Caribbean coast (Lara-Hernandez et al., 2024).

Multidisciplinary efforts have been undertaken to develop Sargassum forecasting systems at basin and seasonal scales, mainly focused on the tropical Atlantic (Berline et al., 2020; Jouanno et al., 2021, 2023). In the Mexican Caribbean, observational and satellite-based studies have quantified Sargassum landing volumes (Arellano-Verdejo et al., 2025; Rodriguez-Martinez et al., 2022; Uribe-Martinez et al., 2022), while numerical modelling studies have investigated the drivers of Sargassum transport and beaching at temporal scales of approximately 10 days and spatial scales of a few kilometres (Lara-Hernandez et al., 2024). Nevertheless, an operational short-term Sargassum forecasting system for the Mexican Caribbean remains pending.

High-resolution ocean models may be required to accurately reproduce the circulation processes that modulate nearshore Sargassum transport, as small-scale circulation features may play a critical role in its transport and accumulation. However, such models are computationally expensive and may be impractical for operational forecasting systems. To determine whether high-resolution models are necessary to forecast Sargassum beaching events we adopted a Lagrangian approach; specifically, we simulated the dispersal of Sargassum along the Mexican Caribbean coastline using current fields modelled at 1 and 5 km resolutions and compared Sargassum final distributions, landings, and pathways.

### 1.1 Study area

The Mexican Caribbean is located on the western side of the Caribbean Sea, within the Yucatan Basin. The main oceanic current in the region, the Cayman Current, flows westward at approximately 19°N until it encounters the Yucatan Peninsula, where it turns northward and becomes the Yucatan Current (Badan Jr et al., 2005; Carrillo et al., 2015; Centurioni and Niiler, 2003; Cetina et al., 2006; Ezer et al., 2005; Ochoa et al., 2005). The latitude at which the Cayman Current encounters the Yucatan Peninsula and gives rise to the Yucatan Current varies by approximately 2°, migrating from the Mexico–Belize border (18°N) to the vicinity of Cozumel (20°N) over time scales of about 100 days (Badan Jr et al., 2005; Cetina et al., 2006). This displacement, together with the presence of mesoscale structures such as eddies, modulates the intensity and structure of the regional currents (Badan Jr et al., 2005; Cetina et al., 2006; Ezer et al., 2005).

The northward flowing Yucatan Current dominates the circulation along the west coast of the Yucatan Peninsula; it intensifies as it flows and reaches maximum speeds of 2 m/s within the Yucatan Channel (Badan Jr et al., 2005; Cetina et al., 2006). On the eastern edge of the Yucatan Channel there is an intermittent southward flow associated with the Cuban Countercurrent (Candela et al., 2002; Ochoa et al., 2001; Sheinbaum et al., 2002).

At Cozumel, the Yucatan Current bifurcates, with approximately one quarter of its flow crossing the Cozumel Channel (Badan Jr et al., 2005). Within the channel, the flow is predominantly geostrophic, although ageostrophic periods lasting approximately

https://doi.org/10.5194/egusphere-2026-3754
Preprint. Discussion started: 2 July 2026


one week have been reported (Ezer et al., 2005; Ochoa et al., 2005; Cetina et al., 2006; Chavez et al., 2003). Current speeds in the central part of the Cozumel channel range from 0.2 to 1.8 m/s (Ochoa et al., 2005).

South of Banco Chinchorro and toward the Gulf of Honduras, current speeds are approximately an order of magnitude smaller than those of the Yucatan Current. In the Gulf of Honduras, the Honduras Gyre is present, a mesoscale cyclonic eddy with a diameter of approximately 200 km (Ezer et al., 2005; Carrillo et al., 2015). The intensity of cyclonic circulation in this region is influenced by the interaction of mesoscale eddies and the proximity of the Cayman Current to the Yucatan Peninsula (Ezer et al., 2005).

South of Cuba, the flow is weak and dominated by eddies (Centurioni and Niiler, 2003; Ochoa et al., 2001). Circulation in this region is predominantly anticyclonic, with frequent formation of anticyclones that propagate westward at speeds of approximately 0.02 m/s (Jouanno et al., 2008). Southwest of Cuba, the formation of cyclone-anticyclone pairs with characteristic diameters of about 100 km has been reported; these eddies propagate toward the Yucatan Current and are eventually incorporated into it (Richardson, 2005).

In the Yucatan Basin, winds are generally weaker than in other regions of the Caribbean Sea. They predominantly blow from the east during spring and summer, and from the northeast during autumn and winter (Pérez-Santos et al., 2010). Wind speeds are largest in autumn and decrease during the subsequent seasons, with a relative maximum in June (Pérez-Santos et al., 2010; Muñoz et al., 2008). Wind patterns in the region are strongly influenced by tropical storms and cyclones. The frequency of tropical cyclones exhibits a minimum in July and two maxima in June and October (Inoue et al., 2002). In addition, during autumn and winter, wind direction is affected by cold fronts originating in North America. These frontal systems occur at intervals of approximately 2 to 16 days and are associated with low-pressure systems that propagate eastward across the Gulf of Mexico (Pérez-Santos et al., 2010; Fernandez-Partagas and Mooers, 1975).

The coexistence of strong currents, mesoscale eddies, island-induced recirculation, and intense atmospheric forcing events makes the Mexican Caribbean a complex, dynamic region where multiscale processes are expected to strongly influence the Lagrangian transport and coastal accumulation patterns.

https://doi.org/10.5194/egusphere-2026-3754
Preprint. Discussion started: 2 July 2026


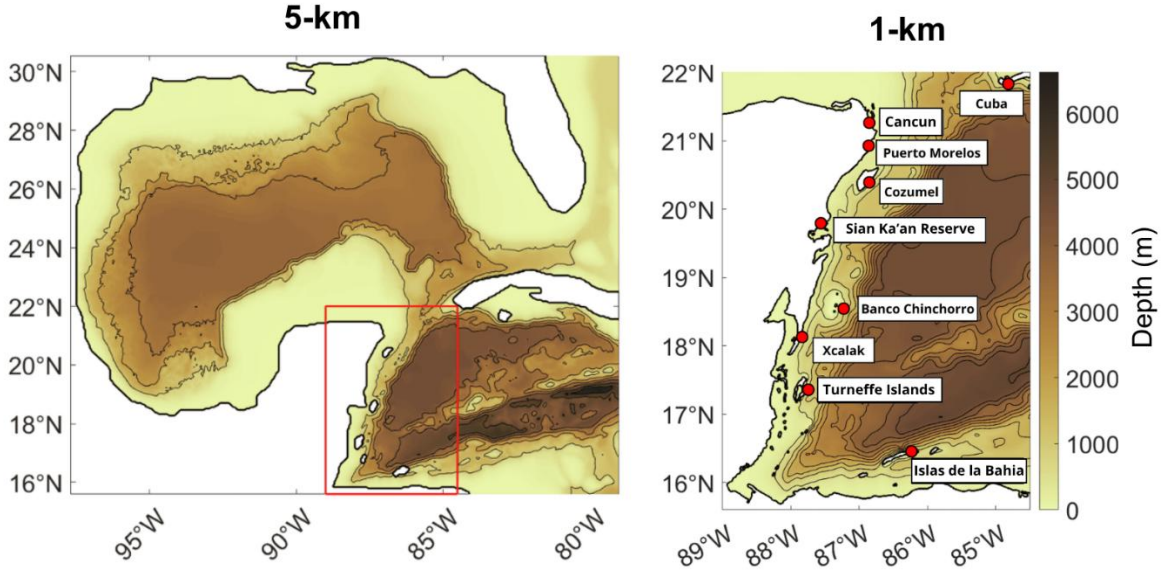


**Fig. 1: ROMS simulation domains at 5-km (left panel) and 1-km (right panel) horizontal resolution. The study area corresponds to the 1-km domain, within which relevant locations are labelled.**

## 2 Methods

Sargassum transport was simulated through the advection of Lagrangian particles using the OpenDrift model (Dagestad et al., 2018). Particles were advected by both ocean currents derived from the Regional Ocean Modeling System (ROMS) configured with 5-km and 1-km spatial resolutions, and wind fields from the fifth-generation reanalysis for the global climate and weather (ERA5; Hersbach et al., 2023). ROMS is a free-surface, four-dimensional (3 spatial coordinates and time) regional numerical model that solves the primitive equations under the hydrostatic and Boussinesq approximations; it uses orthogonal curvilinear coordinates in the horizontal and terrain-following sigma coordinates in the vertical (Shchepetkin and McWilliams, 2005; Shchepetkin and McWilliams, 2009). Simulations were carried out in the domains shown in Fig. 1.

The larger domain (Fig. 1, left panel), with a 5-km resolution, extends from 15.6° to 30.5°N and from 79° to 98°W. It uses 36 vertical sigma levels, with surface-focused stretching and the KPP vertical mixing scheme (Large et al., 1994). It was forced with atmospheric fields from ERA5 (1/4° x 1/4°, hourly) and with initial and boundary oceanic conditions from the Operational Mercator global ocean analysis and forecast system (1/12° x 1/12°, daily; Copernicus Marine Service, 2026). The smaller domain (Fig. 1, right panel), with a 1-km resolution, covers the area from 15.6° to 22°N and from 84.5° to 89°W. It has 45 vertical sigma levels, with vertical stretching parameters and KPP mixing scheme consistent with those used in the 5-km configuration. This simulation was nested within the 5-km simulation, using atmospheric forcing from ERA5 (1/4° x 1/4°, hourly) and initial and boundary conditions from the 5-km ROMS output (5 km x 5 km, every 12 hours). Both simulations span the period from August 1, 2022, to July 27, 2023.

https://doi.org/10.5194/egusphere-2026-3754
Preprint. Discussion started: 2 July 2026


Surface ocean currents from these simulations were used to configure the particle tracking in OpenDrift, a Python-based tool for modeling Lagrangian particle trajectories. OpenDrift enables the advection of particles using oceanic and atmospheric data from various sources (Dagestad et al., 2018). To simulate Sargassum transport, particle advection simulations were conducted using daily surface ocean currents from both the 5-km and 1-km outputs, along with wind fields (zonal and meridional components at 10 m) from ERA5 (1/4° x 1/4°, hourly).

Particle advection velocity was given by the following equation:

$$\boldsymbol{u}(\boldsymbol{x},t) = \boldsymbol{u_o}(\boldsymbol{x},t) + \alpha \boldsymbol{u_w}(\boldsymbol{x},t) \quad (1)$$

Where $t$ is time, $\boldsymbol{x}$ is the position vector of the particle, $\boldsymbol{u}$ is the total advection velocity, $\boldsymbol{u_o}$ is the surface ocean current velocity, $\boldsymbol{u_w}$ is the 10-m wind velocity, and $\alpha$ is the dimensionless windage factor coefficient. Studies modelling Sargassum dispersal have used windage factors ranging from 0.5% to 3% (Berline et al., 2020; Lara-Hernandez et al., 2024; Putman et al., 2020; Putman et al., 2018; Johns et al., 2020; Johnson et al., 2020; Podlejski et al., 2023). In this study, a windage factor of 2.5% was applied to particle advection, based on a sensitivity analysis comparing simulated particle trajectories with trajectories of undrogued buoys from the NOAA Global Drifter Program (Lumpkin and Centurioni, 2019), as it has been suggested that the transport of these buoys is similar to that of Sargassum mats (Beron-Vera et al., 2022; van Sebille et al., 2021). A detailed description of this analysis is presented in Appendix A.

### 2.1 Case study description

To assess the impact of spatial resolution on the development of short-term operational forecasting systems for Sargassum beaching, we selected four ten-day case studies to evaluate differences in particle transport between simulations forced by surface ocean current fields with horizontal resolutions of 5 km and 1 km. The selected periods represent contrasting dynamical regimes in the Mexican Caribbean, allowing assessment of resolution sensitivity under different environmental conditions and circulation patterns.

The first case (Mean Circulation; 7–17 August 2022) is characterized by circulation patterns representative of the annual mean conditions. This case was selected to examine Sargassum transport under typical background flow. The second case (Tropical Cyclone; 1–11 November 2022) captures the passage of Tropical Cyclone Lisa across the region and was selected to assess Sargassum transport during extreme weather events. The third case (Large Ro; 30 March–9 April 2023) features an intensified cyclonic circulation south of the core of the Cayman Current and is characterized by a high Rossby number not associated with enhanced wind speed. This case was selected to investigate particle transport under conditions of increased relative vorticity. The fourth case (Anticyclonic Eddy; 10–20 June 2023) is defined by the presence of an anticyclonic eddy south of Cuba and was included to investigate the role of coherent mesoscale structures modulating particle retention, dispersion, and downstream transport.

https://doi.org/10.5194/egusphere-2026-3754
Preprint. Discussion started: 2 July 2026


These cases were selected with the assumption that enhanced wind forcing or complex ocean circulation promote the development of small-scale features. Collectively, they allow for a comparison of particle transport and landing between model resolutions, and assessing whether higher-resolution simulations capture additional features that influence particle landing timing and spatial distribution.

#### 2.1.1 Simulation configuration for assessing particle landing timing and location

To analyse particle landing distributions in each of the four cases, 9,000 particles were released every 6 h for 10 days along a line at 85°W, extending from 16° to 22°N, ensuring adequate coverage of the study area. This release configuration represents particles entering the domain from the Caribbean Sea, the diagnosed entryway of Sargassum into our study area. Ocean currents were updated every 6 h, and wind fields were updated hourly. Particle trajectories were computed using a fourth-order Runge-Kutta integration scheme with a 300 s time step, and outputs were generated every 6 h.

At the end of each simulation (after 10 days of advection of the first set of released particles in day 1), particles were classified into three categories: (i) active particles remaining within the domain, (ii) stranded particles, and (iii) particles exiting the model domain. A particle was considered stranded when it crossed the 50 m isobath, which was used as a proxy for nearshore accumulation. The percentage of particles in each category was calculated for comparison between resolutions.

A diffusive term was not included, as the aim of the study was to assess the influence of ocean currents spatial resolution on Sargassum advection. Thus, implementing diffusion to parameterize smaller spatial scale circulation is deemed unnecessary.

### 2.2 Finite-time Lyapunov exponents (FTLE) fields

To assess and compare the dispersion pathways of Lagrangian particles between the 5 km and 1 km model outputs, forward and backward finite-time Lyapunov exponent (FTLE) analyses were performed. This methodology allows for the assessment of particle dispersion as they are transported at the ocean surface and aids in the identification of transport structures, which may further suggest probable locations of stranding sites. To construct the FTLE fields, 339 × 229 particles were released on a uniform grid with 2 km spacing covering the entire study area. Particles were advected using surface currents and a windage factor of 2.5%, and a free-slip boundary condition was applied at the coast to ensure continuous FTLE fields.

Forward and backward FTLE fields were computed for each case by seeding particles on the regular grid and advecting them for 10 days using a time step of 300 s. For the forward simulations, particles were initialized on the first day of each case and integrated forward in time for 10 days. Conversely, for the backward simulations, particles were initialized on the last day of each case and integrated backward in time for 10 days.

FTLE provide a measure of the maximum separation rate between trajectories over a finite time interval (Peng et al., 2024). To compute these rates, particles are initially distributed on a uniform grid with positions X0 at time t0. The particles are then

https://doi.org/10.5194/egusphere-2026-3754
Preprint. Discussion started: 2 July 2026


advected over a time T, and the resulting deformation of fluid parcels is quantified using the Cauchy-Green strain tensor. The FTLE at each point is derived from the largest eigenvalue of this tensor, following the formulation of Haller (2001):

$$\sigma_{t_0}^{T} = \frac{1}{|T|}\ln(\lambda_{max}) \quad (2)$$

Where $\sigma^{T}_{t0}$ is the FTLE, $\lambda_{max}$ is the maximum eigenvalue of the Cauchy-Green strain tensor, and $T$ is the duration. Forward FTLE fields highlight repelling structures, where the highest FTLE values indicate regions of maximum trajectory divergence. In contrast, backward FTLE fields reveal attractive structures, with maxima corresponding to regions where trajectories converge when traced backward in time (Peng et al., 2024).

### 2.3 Metrics for assessing particle landings

To quantify the number of active, stranded, and out-of-domain particles at the end of each simulation and to identify the locations most susceptible to particle stranding, the percentage of stranded particles within each 1/4° grid cell and for each case was calculated. This percentage was obtained by dividing the number of stranded particles in each cell by the total number of stranded particles for that case. Additionally, for each particle release event (every 6 h during 10 days), the percentage of stranded particles was computed at the end of the simulation (i.e., 10 days after the first release on day 1) to compare the stranding percentage and to identify the largest difference in strandings among all release events between the 5-km and 1-km configurations. To determine the time it took particles to reach the coastline, we calculated the mean stranding time (days from release) for each 1/4° grid cell and case.

## 3 Results

### 3.1 FTLE

To identify attraction and repelling structures in the 5- and 1-km configurations, forward and backward FTLE fields were analysed for each case.

In the Mean Circulation case, maximum values of the forward FTLE fields, which highlight typical particle pathways along which they are advected rapidly, are located along the northern edge of the Cayman/Yucatan Current in both grids (Fig. 2a). In the 1-km grid (Fig. 2b), this region exhibits stronger instabilities compared to the 5-km grid. In the 5-km grid, the fields indicate a direct flow toward Cozumel, whereas in the 1-km grid, meanders and lower FTLE values are observed. Both grids show high FTLE values outlining a path from the southeastern part of the domain below the Cayman Current to the Islas de la Bahia, suggesting a route for particle transport and potential landings on these islands. In the Gulf of Honduras, FTLE values are lower than in the Cayman Current region, with numerous filaments present. Additionally, in the 5-km grid, elevated FTLE

https://doi.org/10.5194/egusphere-2026-3754
Preprint. Discussion started: 2 July 2026


values extend from the Cayman Current toward Xcalak, suggesting a pathway for particle landings that is less pronounced in the 1-km grid.

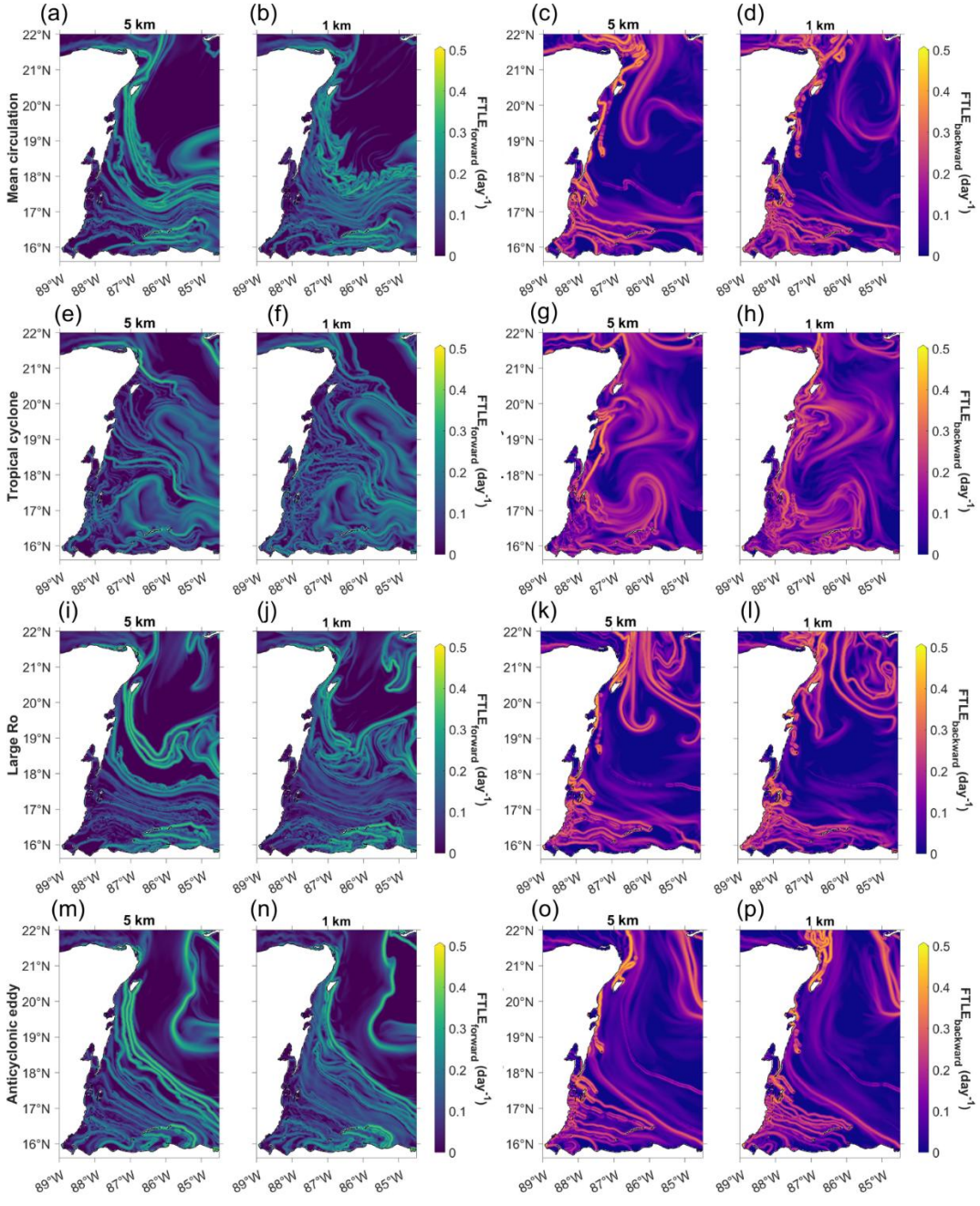


**Fig. 2: Finite-time Lyapunov exponent (FTLE) fields computed for forward and backward integrations using surface ocean currents at 5-km and 1-km spatial resolution. For the 5-km and 1 km configurations respectively, forward simulations correspond to panels (a, b) Mean Circulation, (e, f) Tropical Cyclone, (i, j) Large Ro, and (m, n) Anticyclonic Eddy, while backward simulations correspond to panels (c, d) Mean Circulation, (g, h) Tropical Cyclone, (k, l) Large Ro, and (o, p) Anticyclonic Eddy.**

https://doi.org/10.5194/egusphere-2026-3754
Preprint. Discussion started: 2 July 2026


Backward FTLE fields, which highlight particle accumulation areas, show high values around and north of Cozumel in both grids (Fig. 2c, 2d). The main difference is the appearance of an attractive structure suggesting the presence of a mesoscale eddy in the 1-km grid, absent in the 5-km grid. Previous studies have shown that mesoscale eddies can be identified by analysing FTLE fields (Beron-Vera et al., 2008). Furthermore, mesoscale eddies have been identified as attractive structures that transport Sargassum (Andrade-Canto et al., 2022; Sosa-Gutierrez et al., 2025). The appearance of this structure in the 1-km grid suggests more particle retention in this configuration compared to the 5-km grid. Instead of an eddy-like structure, the 5-km FTLE fields show a region of high values extending from the Caribbean into the Gulf of Mexico that meanders southeast of Cozumel. Both grids exhibit numerous attractive filaments in the Gulf of Honduras. Moreover, Banco Chinchorro appears to induce attractive filaments that may influence particle landings along the coast.

In the Tropical Cyclone case, forward FTLE fields indicate a weakened Cayman Current in both grids (Fig. 2e, 2f), exhibiting meanders and filaments; the appearance of these structures is more evident in the 1-km grid compared to the 5-km grid. In the 5-km grid, a high-value filament extends toward Cancun; a corresponding filament is present in the 1-km grid but with lower FTLE values. Similarly, the 5-km grid shows a high-value filament from the Caribbean toward Xcalak, which is absent in the 1-km grid due to the presence of numerous lower-value filaments.

Backward FTLE fields reveal a dipole-like structure in both grids (Fig. 2g, 2h), more pronounced in the 5-km configuration. This structure, centred around 18.9°N, appears to form two eddies, one north and another south. In the 5-km grid, an attractive filament extends from Cozumel toward the Gulf of Mexico and then west along the northern coast of the Yucatan Peninsula, whereas in the 1-km grid, the filament extends north from Cozumel into the Gulf of Mexico without westward deviation once it crosses Yucatan Channel. Additionally, the 5-km grid exhibits an attractive front with high values east of Xcalak, which is weaker and closer to the coastline in the 1-km grid. Both grids display numerous filaments around the Islas de la Bahia, in the Gulf of Honduras, and high-value filaments near Cuba.

In the Large Ro case, forward FTLE fields exhibit high values along the northern edge of the Cayman Current towards Cozumel in both grids (Fig. 2i, 2j). These values are higher in the 5-km grid than in the 1-km grid, and in the 5-km grid the Cayman Current shows numerous filaments and instabilities. South of Cuba, high-value filaments are observed in both grids; these are more pronounced in the 1-km grid, which may indicate circulation around Cuba. In both grids, filaments originate southeast of the Islas de la Bahia and extend towards the Turneffe islands. In the Gulf of Honduras, FTLE values are low in both grids, although numerous filaments are present. In the 5-km grid, some filaments show higher values than in the 1-km grid, delineating pathways towards Banco Chinchorro and northwards along the coast through the Banco Chinchorro channel.

https://doi.org/10.5194/egusphere-2026-3754
Preprint. Discussion started: 2 July 2026


Backward FTLE fields display high values in both grids (Fig. 2k, 2l) within the Gulf of Honduras, associated with filaments originating from the Islas de la Bahia and reaching the coasts south of Xcalak. High-value filaments also emerge from Banco Chinchorro towards the north in both grids. From Cozumel, high values extend towards the Gulf of Mexico; in the 1-km grid, these filaments reach westward along the northern coast of the Yucatan Peninsula. High FTLE values are also observed in the Yucatan Channel in both grids. South of Cuba, high-value filaments appear in both grids, likely induced by the presence of eddies.

In the Anticyclonic Eddy case, forward FTLE fields in both grids (Fig. 2m, 2n) exhibit maxima along the boundary of the anticyclonic eddy located south of Cuba. Both grids also show elevated FTLE values along the Cayman Current, suggesting a pathway from the Caribbean toward Cozumel; consequently, the highest percentage of stranded particles would be expected around Cozumel, reflecting this direct transport path. Elevated values are also observed extending toward the Islas de la Bahia from the southeast. In the Gulf of Honduras, FTLE values are lower, with numerous filaments present in both grids.

Backward FTLE fields reveal high values around and north of Cozumel in both grids (Fig. 2o, 2p). Banco Chinchorro and its northern region exhibit elevated FTLE values, particularly in the 5-km grid, suggesting that strandings are more likely in this region in the coarser-resolution simulation.

### 3.2 Percentage of stranded particles

For all cases, the stranded particle percentage (SP%) decreased with release time (Fig. 3a–d). According to Lara-Hernandez et al. (2024), particles seeded approximately 160 km offshore from the coastline (between 86 and 86.5°W) require about 7–8 days to reach the Mexican Caribbean coast. Therefore, the reduction in SP% with increasing release time can be attributed to particles not being advected enough time to reach the coastline but still active within our study domain. In general, particles released after day 5 did not reach the coast, except for a fraction below 3% in the Tropical Cyclone, Large Ro, and Anticyclonic Eddy cases (Fig. 3b–d). Given this low percentage and the offshore release distance relative to the Yucatan Peninsula, these strandings likely occurred along the coasts of the Islas de la Bahia or Cuba which are closer to the release location.

The maximum SP% values occurred at the earliest release time in all cases (Fig. 3a–d), likely reflecting the longer available transport time for particles to reach the coast. For the earliest release, in the Mean Circulation case, SP% reached approximately 25% for both grids (Fig. 3a). For the Tropical Cyclone case, maximum values were 34% for the 1-km grid and 44% for the 5-km grid (Fig. 3b). In the Large Ro case, SP% peaked at 40% for the 5-km grid and 44% for the 1-km grid (Fig. 3c), while in the Anticyclonic Eddy case, values for the 5- and 1-km grids were 29% and 25%, respectively (Fig. 4c). The largest differences between grid configurations occurred in the Tropical Cyclone case (Fig. 3b), with a maximum difference of approximately 23% (Fig. 3b). In the remaining cases, the maximum difference between grids was smaller than 7.5% (Fig. 3a, 3c, 3d).

https://doi.org/10.5194/egusphere-2026-3754
Preprint. Discussion started: 2 July 2026


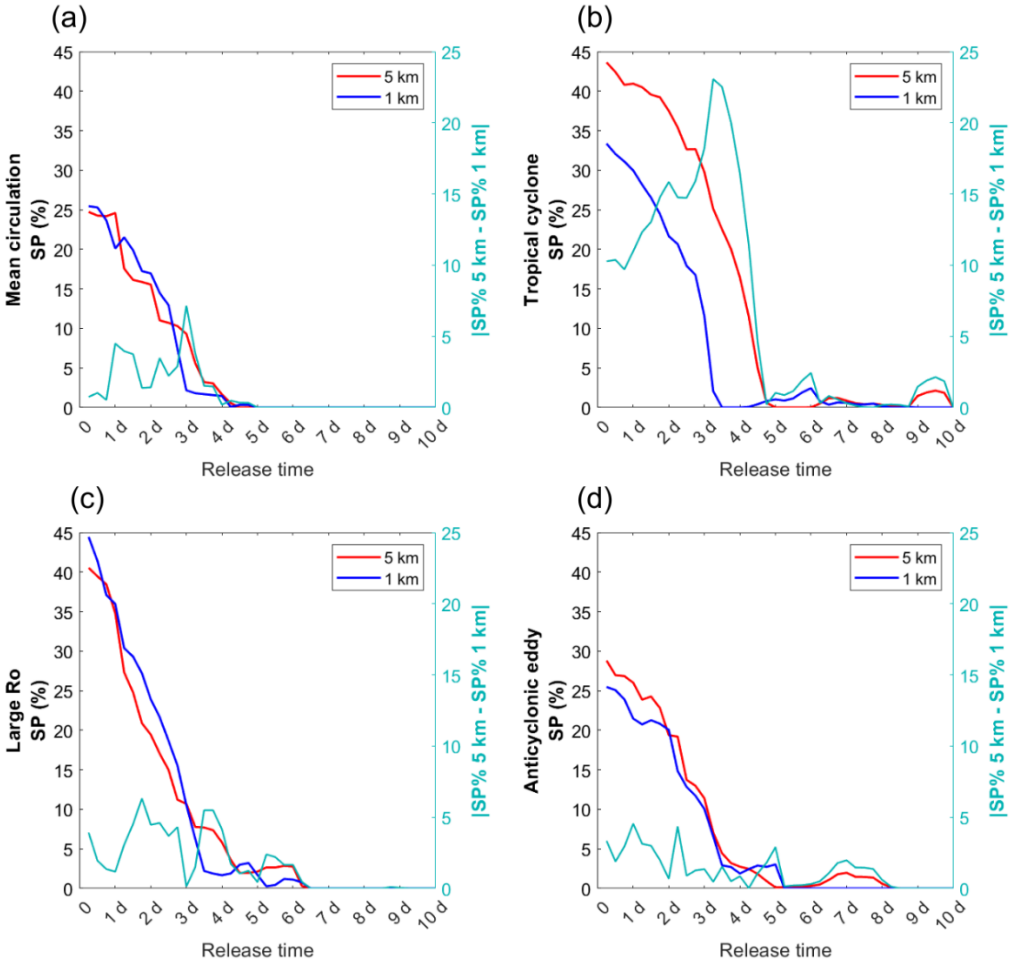


**Fig. 3: Particle percentages per release time for the Mean Circulation (a), Tropical Cyclone (b), Large Ro (c), and Anticyclonic Eddy (d) cases. Results are shown for particles advected using the 5-km (red) and 1-km (blue) configurations. The difference between the 5-km and 1-km percentages is shown in cyan.**

For the Mean Circulation case, the percentages of active, stranded, and out-of-domain particles relative to the total number of particles released, were 71.45%, 5.46%, and 23.10%, respectively in the 5-km grid, while in the 1-km grid, these values were 72.02%, 5.36%, and 22.62%, respectively (Table 1). Areas with a higher percentage of particle landings (>8%) in the 5-km grid were located around the Islas de la Bahia, Chinchorro Bank, and Cozumel (Fig. 4a). In the 1-km grid, the highest landing percentages (approximately 7%) occurred around Chinchorro Bank and the Sian Ka'an Reserve (Fig. 4b). The most significant differences in landing percentage (>6%) were observed around Cozumel, the Sian Ka'an Reserve, and Chinchorro Bank (Fig. 4c), although this last location had the highest landing % at both resolutions (Fig. 4a,b).

https://doi.org/10.5194/egusphere-2026-3754
Preprint. Discussion started: 2 July 2026


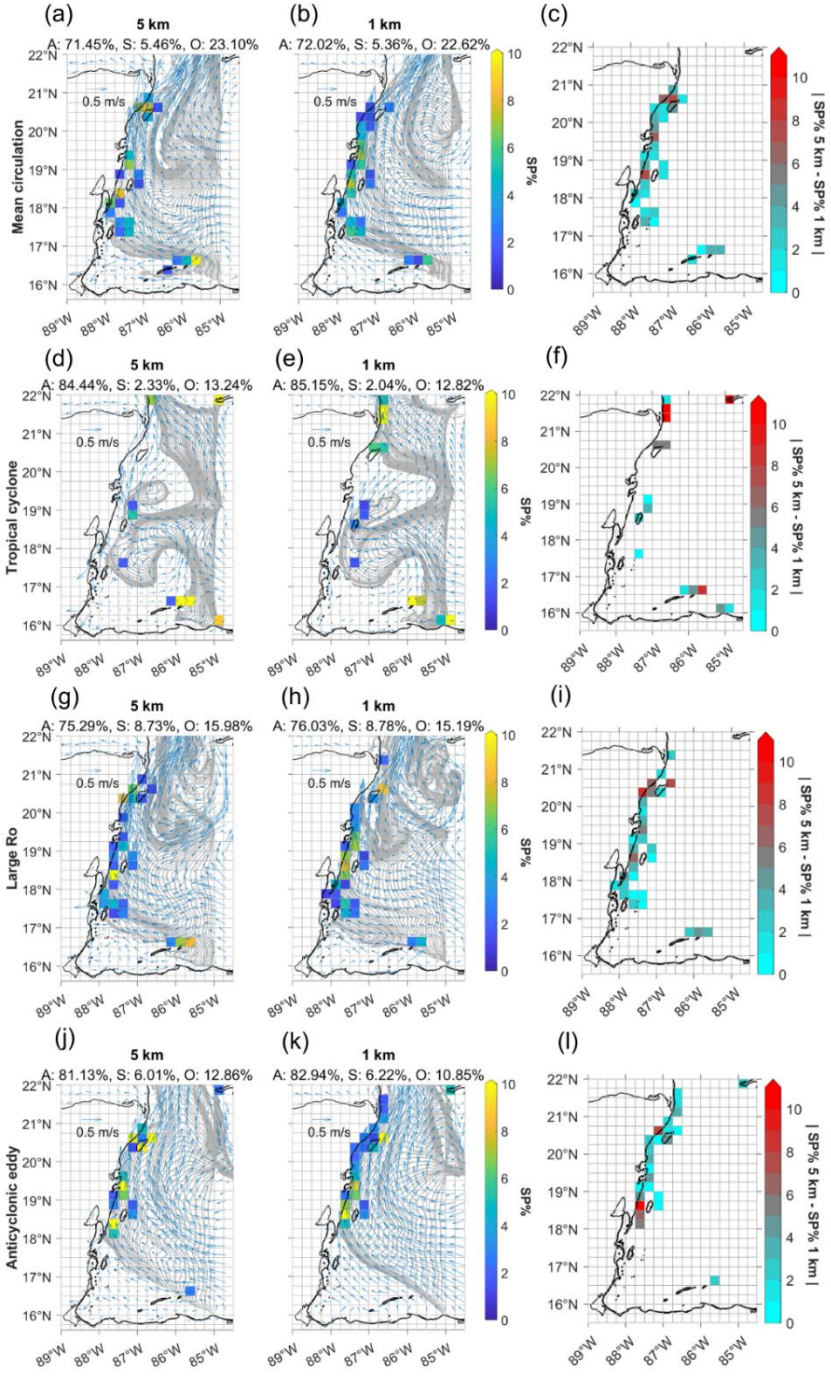


**Fig. 4: Stranded particle percentage (SP%) in each 1/4° grid cell at the end of the simulation period, using the 5-km and 1-km ROMS configurations. Results for the 5-km and 1-km grids and their absolute difference are respectively shown in panels (a, b, c) Mean Circulation, (d, e, f) Tropical Cyclone, (g, h, i) Large Ro, and (j, k, l) Anticyclonic Eddy. The total percentages of active (A), stranded (S), and out-of-domain (O) particles are indicated. Gray dots denote the final positions of individual Lagrangian particles, and the vector field represents the mean surface ocean currents for each case.**

https://doi.org/10.5194/egusphere-2026-3754
Preprint. Discussion started: 2 July 2026


| Case | Resolution | Percentages of active (%A), out-of-domain (%O), and stranded (%S) particles at the end of the simulation | | | Difference of %S between 5- and 1-km outputs | Largest difference of %S between 5- and 1-km outputs among release times | Location(s) of largest difference of %S per grid cell |
|---|---|---|---|---|---|---|---|
| | | % A | % O | % S | | | |
| Mean Circulation | 5 km | 71.45 | 23.10 | 5.46 | 0.10 | 7.14 | Cozumel, Sian Ka'an Reserve, Banco Chinchorro |
| | 1 km | 72.02 | 22.62 | 5.36 | | | |
| Tropical Cyclone | 5 km | 84.44 | 13.24 | 2.33 | 0.29 | 23.06 | Cuba, Islas de la Bahia, north of Cancun |
| | 1 km | 85.15 | 12.82 | 2.04 | | | |
| Large Ro | 5 km | 75.29 | 15.89 | 8.73 | 0.05 | 6.31 | Cozumel |
| | 1 km | 76.03 | 15.19 | 8.78 | | | |
| Anticyclonic Eddy | 5 km | 81.13 | 12.86 | 6.01 | 0.21 | 4.35 | Cozumel, Banco Chinchorro |
| | 1 km | 82.94 | 10.85 | 6.22 | | | |

**Table 1. Percentages with respect to total particles released of active (%A), out-of-domain (%O), and stranded (%S) particles at the end of the simulation; differences in %S between the 5- and 1-km outputs; largest %S difference between the 5- and 1-km outputs across release times; and location(s) of the largest difference of %S per grid cell, for each case in the 5- and 1-km model configurations.**

In the Tropical Cyclone case, the percentages of active, stranded, and out-of-domain particles in the 5-km grid were 84.44%, 2.33%, and 13.24%, respectively, while in the 1-km grid, these values were 85.15%, 2.04%, and 12.82%, respectively (Table 1). Areas with a higher percentage of particle landings (>8%) in both grids were located around the Islas de la Bahia (Fig. 4d, 4e). In the 5-km grid, additional concentrations were observed near the southeastern coast of Cuba (Fig. 4d), while in the 1-km grid, they occurred north of Cancun (Fig. 4e). The largest differences in landing percentage (>10%) were recorded in Cuba, the Islas de la Bahia, and north of Cancun (Fig. 4f).

https://doi.org/10.5194/egusphere-2026-3754
Preprint. Discussion started: 2 July 2026


In the Large Ro case, the percentages of active, stranded, and out-of-domain particles in the 5-km grid were 75.29%, 8.73%, and 15.98%, respectively, while in the 1-km grid, these values were 76.03%, 8.78%, and 15.19%, respectively (Table 1). Areas with a high percentage of particle landings (>8%) in both grids were located around Cozumel and Chinchorro Bank (Fig. 4g, 4h), and in the Islas de la Bahia in the 5-km grid (Fig. 4g). The largest differences in landing percentage (>10%) were recorded around Cozumel (Fig. 4i).

In the Anticyclonic Eddy case, the percentages of active, stranded, and out-of-domain particles in the 5-km grid were 81.13%, 6.01%, and 12.86%, respectively, while in the 1-km grid, these values were 82.94%, 6.22%, and 10.85%, respectively (Table 1). Areas with a higher percentage of particle landings (>8%) in both grids were located around Cozumel, Chinchorro Bank, and the Sian Ka'an Reserve (Fig. 4j, 4k). The largest differences in landing percentages (>10%) were observed within the Cozumel and Chinchorro channels (Fig. 4l).

The mean percentages across cases of active, stranded, and out-of-domain particles across all four cases were 78.08%, 5.63%, and 16.30%, respectively, for the 5-km grid, and 79.04%, 5.60%, and 15.37%, respectively, for the 1-km grid (Table 1). The highest stranding percentages were observed in the Large Ro case (8.73% and 8.78%) and the lowest in the Tropical cyclone (2.33% and 2.04%). The low percentage in the Tropical cyclone case might be attributed to the weakening of pathways towards the coast due to the generation of submesoscale features as evidenced by FTLE fields (Fig. 2e, 2f); these submesoscale features may prolong the advection time of particles towards the coast causing a higher percentage of active particles for this case.

### 3.3 Mean stranding time

In the Mean Circulation case, the mean stranding time around Cozumel was 8 days in the 5-km grid (Fig. 5a) and 7 days in the 1-km grid (Fig. 5b); around Banco Chinchorro and the Turneffe Islands, the mean stranding time was 6 days in both grids; and in the Islas de la Bahia, the values were 7 days in the 5-km grid and 8 days in the 1-km grid. Differences in mean stranding time between the 5-km and 1-km grids were as large as 5 days and constrained to grid cells where stranding only occurred at low or high resolution. For those grid cells where stranding occurred at both resolutions the difference in mean stranding time was of 1.5 days or less (Fig. 5c). Differences between 12 and 24 h occurred around Cozumel, the Sian Ka'an Reserve, and the Turneffe Islands, while differences between 1 and 1.5 days were registered around Islas de la Bahia.

https://doi.org/10.5194/egusphere-2026-3754
Preprint. Discussion started: 2 July 2026


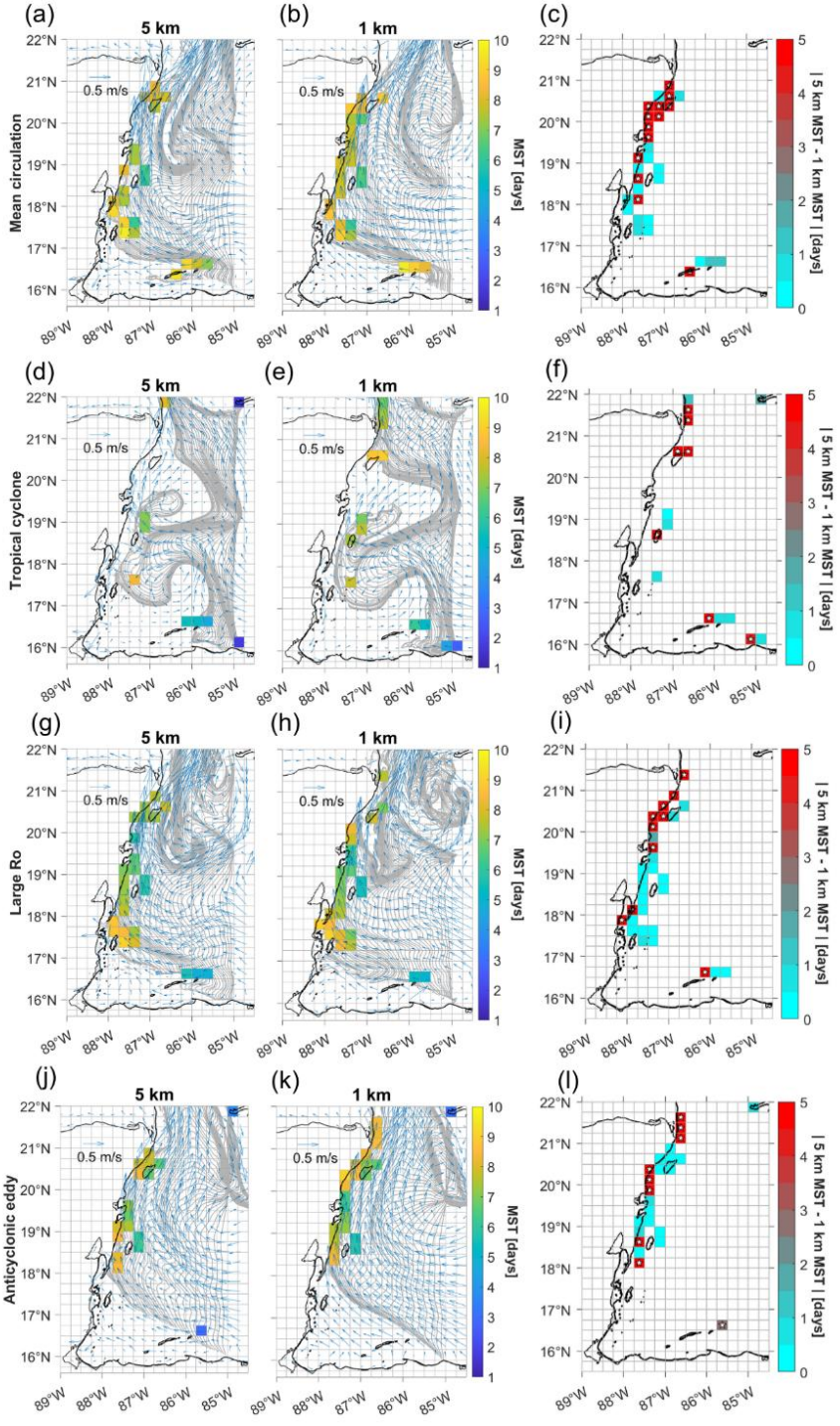


**Fig. 5: Mean particle stranding time (days from release) in each 1/4° grid cell, calculated from Lagrangian particle simulations at 5-km and 1-km resolutions. Results for the 5-km, the 1-km grids and their absolute difference are respectively shown in panels (a, b, c) Mean Circulation, (d, e, f) Tropical Cyclone, (g, h, i) Large Ro, and (j, k, l) Anticyclonic Eddy. Gray dots denote the final positions**

https://doi.org/10.5194/egusphere-2026-3754
Preprint. Discussion started: 2 July 2026


**of individual Lagrangian particles, and the vector field represents the mean surface ocean current field for each case. Cells marked with a star indicate locations where particles land in one configuration but not in the other.**

In the Tropical Cyclone case, the mean stranding time around Cozumel was 8 days in the 1-km grid (Fig. 5e). North of Cancun, the mean stranding time was 8 days in the 5-km grid (Fig. 5d) and 6 days in the 1-km grid. Around Banco Chinchorro, the mean stranding time was 7 days in both grids. In the Turneffe Islands, it was 9 days in the 5-km grid and 8 days in the 1-km grid. In the Islas de la Bahia, the mean stranding time was 4 days in both grids, while in the southeastern boundary of the domain it was 2 days in both grids. Differences between the 5-km and 1-km grids ranged from 12 to 24 hours (Fig. 5f) in cells located in the Turneffe Islands, Islas de la Bahia, Banco Chinchorro, and the southeastern boundary of the domain. Differences of 1 to 1.5 days were observed north of Cancun.

In the Large Ro case, the mean stranding time around Cozumel was 7 days in both grids (Fig. 5g, 5h). Around the Sian Ka'an Reserve, the mean stranding time was 6 days in the 5-km grid and 8 days in the 1-km grid. Around Banco Chinchorro, it was 6 days in both grids. In the Turneffe Islands, the mean stranding time was 8 days in both grids, and in the Islas de la Bahia, it was 5 days in both grids. Near Cancun, the mean stranding time was 7 days in the 1-km grid. Differences in mean stranding time of 12 to 24 hours (Fig. 5i) were observed around Cozumel and the Turneffe Islands, while differences of 1.5 to 2 days were found around the Sian Ka'an Reserve.

In the Anticyclonic Eddy case, the mean stranding time around Cozumel was 6 days in the 5-km grid (Fig. 5j) and 7 days in the 1-km grid (Fig. 5k). In the Sian Ka'an Reserve, it was 7 days in the 5-km grid and 6 days in the 1-km grid. Around Banco Chinchorro, the mean stranding time was 6 days in both grids. Along the Cuban coast, it was 3 days in the 5-km grid and 4 days in the 1-km grid. In the Islas de la Bahia, the mean stranding time was 3 days in the 1-km grid. North of Cancun, the mean stranding time was 9 days in the 1-km grid. Differences in mean stranding time between the 5-km and 1-km grids ranged from 12 to 24 hours (Fig. 5l) in areas around the Sian Ka'an Reserve, Banco Chinchorro, and the Cuban coast.

## 4 Discussion

This study assessed the impact of ocean current spatial resolution (5 and 1 km) on short-term predictions of Sargassum strandings in the Mexican Caribbean using Lagrangian simulations. The results indicate that, despite local differences in stranding patterns, particularly in regions with complex coastal geometry and during extreme events, the dominant transport pathways, stranding percentages and mean arrival times are broadly consistent between the two resolutions. Overall, the findings suggest that 5-km-resolution models are sufficient for operational short-term forecasting, while higher-resolution simulations can provide added spatial detail in specific settings, supporting more effective Sargassum management and mitigation strategies.

https://doi.org/10.5194/egusphere-2026-3754
Preprint. Discussion started: 2 July 2026


The FTLE analysis from trajectories of particles released throughout the domain allowed us to identify persisting transport patterns and landing pathways. According to the overall identified patterns of Sargassum transport into the study area from the eastern Caribbean Sea, the Cayman and Yucatan Currents serve as the main transport pathway, primarily directing particles toward Cozumel (Fig. 2a, 2b, 2i, 2j, 2m, 2n). North of Cozumel, attractive filaments are generated that may indicate enhanced landings in the region (Fig. 2c, 2d, 2g, 2h, 2k, 2l, 2o, 2p). Particle landings around and along Banco Chinchorro are influenced by attractive structures, which appear to be induced by the presence of the bank. Although backward FTLE fields indicate attractive structures in the Gulf of Honduras, the high forward FTLE values along the Cayman and Yucatan Currents indicate they act as a barrier, limiting Sargassum entry into this region. A pathway extending from the southeast toward the coasts of the Islas de la Bahia was also identified, evidencing another typical pathway towards landing for Sargassum entering the Mexican Caribbean (Fig. 2a, 2b, 2i, 2j, 2m, 2n). Additionally, mesoscale eddies may enhance Sargassum retention in the open sea due to their attractive properties (Fig. 2d, 2m, 2n). The presence of extreme events, such as tropical cyclones, have the potential of debilitating the Cayman/Yucatan Current and therefore the path that this current represents for Sargassum transport (Fig. 2e, 2f), resulting in different stranding times and locations as expected under typical conditions.

Allende-Aradia et al. (2023) calculated climatological Lagrangian Coherent Structures (cLCS) from surface ocean currents to identify transport pathways and barriers in the Atlantic Ocean, spanning from the Western Tropical Atlantic to the Central Subtropical Atlantic including the Gulf of Mexico. They found that regions characterized by current intensification formed attractive pathways that acted as barriers of transport across them. In particular, the Yucatan Current was identified as a persistent onshore transport barrier along the Mexican coast between approximately 18°N and 21°N; this barrier, however, was weakened when wind forcing was included, highlighting wind as a key factor controlling particle landings in coastal regions. These results were consistent with those of Lara-Hernandez et al. (2024), who also observed that trajectories reaching the Mexican Caribbean coast tend to follow the Yucatan Current and subsequently spread along the shoreline. In the Mean Circulation, Large Ro, and Anticyclonic Eddy cases, our results also identified the Yucatan Current as a region with high FTLE forward values (Fig. 2a, 2b, 2i, 2j, 2m, 2n), which suggest that it acts as both an along current transport pathway and an onshore thransport barrier as previously observed. Likewise, in many other coastlines with boundary currents, the onshore transport of larvae depends on factors that debilitate or break the predominant alongshore flow (Harrison and Siegel, 2014) as well as on conditions that generate across shore flows such as onshore winds (Caputi et al., 2002) or eddies (Cetina-Heredia et al., 2019; Roughan et al. 2022).

Furthermore, Tropical Cyclone case results indicate that, under conditions of intense wind speeds, the FTLE fields exhibit lower values (Fig. 2e, 2f), and weaker regions of high FTLE compared to other cases (e.g., the Cayman Current pathways). This behaviour suggests that strong winds reduce the strength of repelling structures, and therefore weaken main particle pathways. In our case, FTLE fields were computed considering a 2.5% windage factor, which produced probable particle pathways toward the coast of Cozumel, thereby explaining particle landings in the region. These results support previous

https://doi.org/10.5194/egusphere-2026-3754
Preprint. Discussion started: 2 July 2026


studies (Allende-Arandia et al., 2023; Lara-Hernandez et al., 2024; Uribe-Martinez et al., 2022) which observed that the inclusion of wind enhances particle landings in the region when analysing long-term basin scale cLCSs.

The largest differences in stranding percentages between simulations' resolution occur under tropical cyclone conditions, which are characterized by enhanced wind speeds and deviations from the typical trade-wind direction. Analysis of the FTLE fields (Fig. 2e, 2f) suggests that these differences may be associated with the generation of submesoscale structures induced by strong winds, which weaken the dominant circulation patterns (e.g., the Cayman and Yucatan Currents) and consequently lead to particle transport pathways divergent between the two model configurations.

The areas with the highest percentages of particle landings across all four cases were Cozumel, Chinchorro Bank, the Sian Ka'an Reserve, and the northern coast of Cancun (Fig. 4). In agreement, the FTLE analysis revealed the presence of probable transport pathways towards Cozumel and the presence of attractive filaments around Chinchorro Bank and north of Cozumel, indicating these regions as prone to landings (Fig. 2).

In the satellite-based and modelling study by Jouanno et al. (2025), the Mexican Caribbean was identified as one of the most vulnerable regions to Sargassum influxes, with a non-uniform impact along the coastline; the high landing rates along the Yucatan Peninsula have been attributed to the orientation of the coastline (as the Cayman Current impinges the Yucatan Peninsula perpendicularly), the transport of Sargassum by the Yucatan Current, and prevailing onshore winds that favour strandings (Lara-Hernandez et al., 2024; Uribe-Martinez et al., 2022). Furthermore, Jouanno et al. (2025) showed that Sargassum strandings are higher between 20°N and Cozumel (~20.3°N), in accordance with observations by Chavez et al. (2020) who registered a high prevalence of Sargassum in this area. Our results confirm these patterns, as we registered high landing percentages around Cozumel.

Although south of 20°N, along the Mexican Caribbean, socioeconomic vulnerability to strandings is moderate to low due to the sparse distribution of human settlements in the region, ecosystems are particularly vulnerable (Uribe-Martinez et al., 2022). Previous observational studies have identified the coast at the Sian Ka'an Reserve as an area with high prevalence of Sargassum (Chavez et al., 2020). In this study, we recorded high landing percentages around Chinchorro Bank and the Sian Ka'an Reserve, emphasizing the importance of protecting these areas from future Sargassum influxes.

In Jouanno et al. (2025), the annual Sargassum biomass was estimated from 2018 to 2023; they reported that the coastline from Xcalak to Puerto Morelos receives approximately 100,000 tons of Sargassum biomass per year, the western Cuban coast receives about 40,000 tons, and the Islas de la Bahia receives less than 20,000 tons per year. In agreement, our results registered strandings along the coast from Xcalak to Puerto Morelos (Fig. 4), possibly associated with Sargassum transport by the Yucatan Current and its interaction with onshore winds. The eddy-like structures south of Cuba revealed by FTLE fields suggest that

https://doi.org/10.5194/egusphere-2026-3754
Preprint. Discussion started: 2 July 2026


stranding events along the Cuban coast relate to particle transport by eddies, while relatively straight trajectories of the backward main attractors suggest that strandings in the Islas de la Bahia corresponded to particles released south of the core of the Cayman Current (Fig. 2). Both our modelling results and Jouanno et al. (2025) biomass estimates, suggest that Sargassum landings are primarily modulated by the Cayman/Yucatan Current and that oceanic eddies play an important role in strandings along the Cuban coast.

The areas with the greatest differences in particle landing percentages between the two grids were located around Cozumel, Chinchorro Bank, north of Cancun, and the Sian Ka'an Reserve. These sites are characterized by complex geomorphology, and the differences in shoreline resolution between the grids appear to play a significant role in particle stranding numbers. This suggests that employing a more realistic shoreline representation could improve biomass predictions of Sargassum strandings.

In general, stranding took close to 8 days near Cozumel, 6 days around Banco Chinchorro, 7 days around the Sian Ka'an Reserve, 3 days along the Cuban coast, and 5 days in the Islas de la Bahia. Lara-Hernandez et al. (2024) reported that Sargassum located approximately 160 km offshore (near 86.5°W) reached the coast of Banco Chinchorro in 7 to 8 days; in contrast, although we released particles along the 85°W longitude, ~0.5° upstream, our results indicate stranding times that are shorter by 1 to 2 days in that region. This discrepancy may be attributed to the fact that Lara-Hernandez et al. (2024) advected particles using surface ocean currents derived from a different model, in addition to applying a windage factor of 2% (i.e., 0.5% smaller than in our simulations).

Considering only the cells where strandings occurred at both resolutions, the largest differences in mean stranding time occurred in the Large Ro case, around the Sian Ka'an Reserve, with values ranging from 1.5 to 2 days. Most differences between the 5-km and 1-km grids fell within the range of 12 to 24 hours. Toxic exposure associated with Sargassum generally occurs during the decomposition stage, which starts typically around 48 hours after beaching (Resiere et al., 2023), although it may begin as early as 24 hours under conditions of high temperature and elevated Sargassum biomass (Chavez et al., 2020). Thus, the observed margin of uncertainty of up to 24 hours between model resolutions is acceptable; however, it remains critical that collection efforts begin as early as possible. Current removal guidelines indicate that Sargassum must be collected within the first 72 hours following beaching (Chavez et al., 2020); even though the 24-hour difference between simulations' resolution falls within this 72-hour window, timely intervention remains essential, especially in scenarios of increased Sargassum biomass arrival.

https://doi.org/10.5194/egusphere-2026-3754
Preprint. Discussion started: 2 July 2026


## 5 Conclusions

This study evaluated the influence of ocean current spatial resolution (5 and 1 km) on short-term predictions of Sargassum strandings in the Mexican Caribbean using Lagrangian simulations. The results show that, despite localized differences in stranding patterns, particularly in regions with complex coastal morphology and during extreme events such as tropical cyclones, the dominant transport pathways, stranding percentages, and mean arrival times are largely consistent between both model resolutions. Differences in mean stranding time were generally within 24 hours, and average stranding percentages differed by less than 1%.

The highest stranding percentages were consistently observed around Cozumel, Banco Chinchorro, the Sian Ka'an Reserve, and the northern coast of Cancun, in agreement with previous observational and modelling studies (Chavez et al., 2020; Lara-Hernandez et al., 2024; Jouanno et al., 2025; Uribe-Martinez et al., 2022). FTLE-based analyses indicate that these regions are recurrently exposed to attractive transport pathways associated with the Cayman and Yucatan Currents, mesoscale eddies, and coastal circulation features, which enhance particle retention and promote landings. Due to their exposure to prevailing currents and the orientation of the coastline, these regions are particularly vulnerable to massive Sargassum landings (Lara-Hernandez et al., 2024; Uribe-Martinez et al., 2022).

Our results suggest that for operational and short-term forecasting purposes, using models with a 5 km spatial resolution is sufficient to represent the general distribution and timing of Sargassum strandings in the region. However, in areas with high geomorphological complexity or during extreme events, higher-resolution models (1 km) can provide improvements in spatial accuracy of landings and associated biomass estimates. Additionally, a detailed representation of the coastline is essential in simulations, as it directly influences stranding patterns. Ultimately, this study contributes to the development and optimization of more robust forecasting tools that can aid Sargassum collection and mitigation strategies, thereby minimizing its ecological and socioeconomic impacts in the Mexican Caribbean.

## 6 Appendices

### Appendix A

To validate the Lagrangian particle simulations and determine an appropriate windage factor for the case studies representing Sargassum advection, we compared observed trajectories from undrogued buoys of the NOAA Global Drifter Program (Lumpkin and Centurioni, 2019) with simulated particle trajectories driven by surface ocean currents at 5 km and 1 km spatial resolution. The transport of undrogued buoys has been shown to be comparable to that of floating Sargassum mats, making them a suitable proxy for validation (Beron-Vera et al., 2022; van Sebille et al., 2021). Five drifters located within the study area during the simulation period were selected for this analysis.

https://doi.org/10.5194/egusphere-2026-3754
Preprint. Discussion started: 2 July 2026


For each drifter, 100 particles were released at the surface every 24 h along the observed buoy trajectory and advected for 24 h. Particles were assigned windage factors ranging from 0 to 5%. The simulations were forced using daily surface currents from the 5-km and 1-km ROMS configurations and hourly ERA5 wind fields. Particle positions after each 24 h integration were compared with the corresponding observed buoy locations, and the Liu–Weisberg skill score was computed to quantify the agreement between simulated and observed trajectories (Liu and Weisberg, 2011). This metric is based on the normalized cumulative Lagrangian separation (s):

$$s = \frac{\sum_{i=1}^{N} d_i}{\sum_{i=1}^{N} l_{oi}} \quad \text{(A1)}$$

Where $d_i$ is the separation between the modelled and observed positions at record $i$, $l_{oi}$ is the length of the observed trajectory, and $N$ is the total number of records. Using this separation $s$, the Liu-Weisberg skill score $ss$ for the modelled trajectories is defined as:

$$ss = \begin{cases} 1 - \frac{s}{n}, (s \le n) \\ 0, (s > n) \end{cases} \quad \text{(A2)}$$

Where $n$ is a tolerance threshold. In this study, $n$ was set to 1, so that $ss$ = 1 when the modelled trajectory perfectly matches the observed trajectory, and $ss$ = 0 when the cumulative separation exceeds the cumulative length of the observed trajectory (Dagestad and Röhrs, 2019).

The trajectory comparisons (Fig. A1a–e) show overall agreement between the simulated particle trajectories and the observed buoy paths. The largest discrepancies occur for the buoy traversing the study area between 31 October and 15 November 2022. This period coincides with the passage of tropical cyclone Lisa across the domain, and the increased divergence between simulated and observed trajectories likely reflects the combined effects of enhanced wind forcing, its impact on ocean circulation, and the generation of submesoscale features, particularly in simulations using the 1 km resolution fields.

The mean Liu-Weisberg skill score results (Fig. A1f) indicate that particle trajectories from the 5 km configuration generally exhibit smaller separation from the observed buoy trajectories than those from the 1 km configuration. For each model setup, the maximum skill score was identified as a function of the windage factor, and a value of 2.5% was selected for the Sargassum simulations, as it yields near-maximum skill scores for both resolutions.

https://doi.org/10.5194/egusphere-2026-3754
Preprint. Discussion started: 2 July 2026


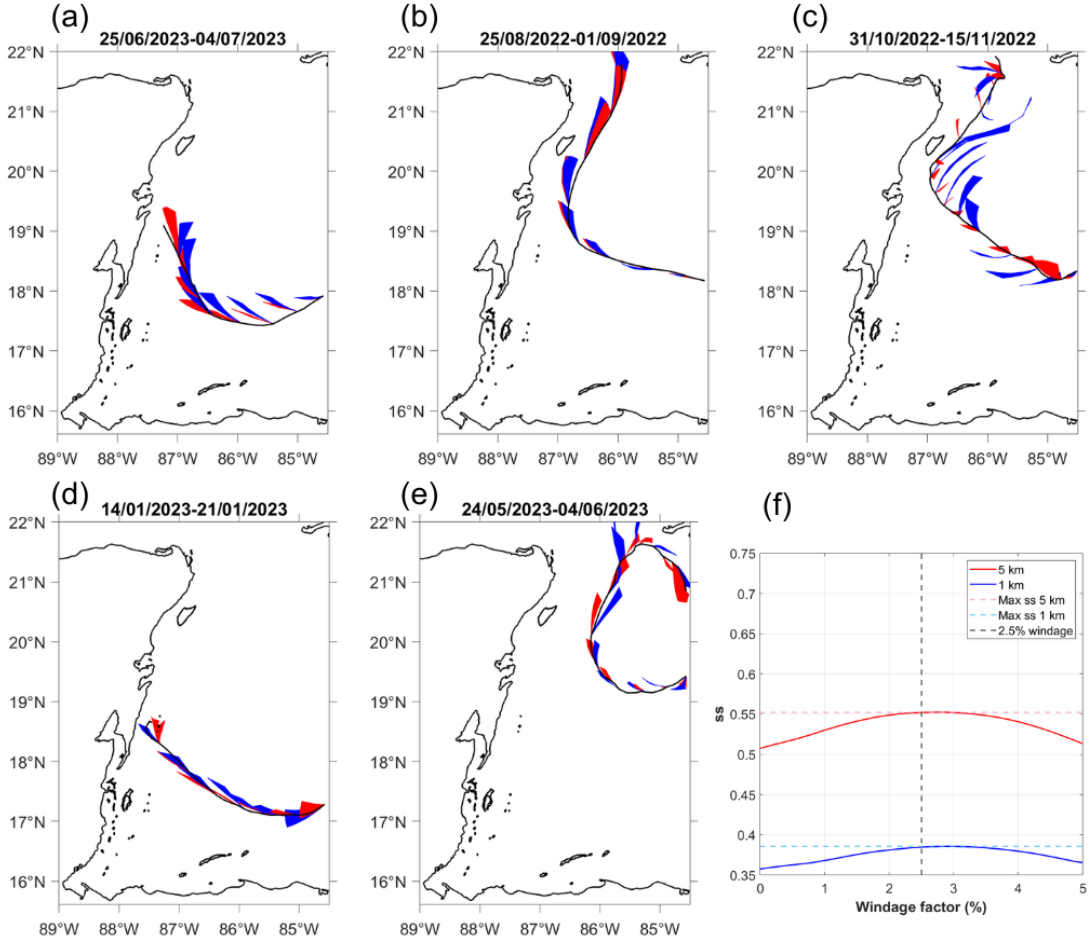


**Fig. A1. Comparison between trajectories of undrogued buoys from the NOAA Global Drifter Program (black lines) and simulated particle trajectories using ocean currents at 5 km (red) and 1 km (blue) horizontal resolution. Panels (a–e) show individual buoy trajectories; for each buoy, 100 particles were released every 24 h along the observed trajectory and advected for 24 h using windage factors ranging from 0 to 5%. After each 24 h integration period, particle positions were compared with the corresponding buoy location, and the Liu–Weisberg skill score (ss) was computed. Panel (f) shows the mean ss as a function of windage factor, where higher (lower) values indicate smaller (larger) separation between observed and simulated trajectories. Solid blue and red lines correspond to the 1 km and 5 km configurations, respectively, while dashed lines indicate the maximum ss achieved by each configuration. The black dashed line marks the 2.5% windage factor adopted in the case study simulations.**

## Code and data availability

The codes and data used in this study are available at https://doi.org/10.5281/zenodo.20787920. ERA5 hourly data is available for download at https://doi.org/10.24381/cds.adbb2d47. NOAA Global Drifter Program quality-controlled 6-hour interpolated data from ocean surface drifting buoys is available for download at https://doi.org/10.25921/7ntx-z961. OpenDrift source code is available at https://doi.org/10.5281/zenodo.845813.

https://doi.org/10.5194/egusphere-2026-3754
Preprint. Discussion started: 2 July 2026


## Supplement link

Not applicable.

## Author contributions

Ana Lucia de Santos Medina performed experiment design, Lagrangian simulations, data analysis and visualization, and writing. Sheila Natali Estrada Allis contributed with experimental and methodological design, data interpretation, and writing. Lorena Guerrero Moreno configured and carried out the hydrodynamic model simulations, as well as contributing to data analysis. Paulina Cetina Heredia contributed with suggestions for data analysis and visualization, the interpretation of results, and writing.

## Competing interests

The authors declare no competing interests.

## Disclaimer

Copernicus Publications remains neutral with regard to jurisdictional claims made in the text, published maps, institutional affiliations, or any other geographical representation in this paper. While Copernicus Publications makes every effort to include appropriate place names, the final responsibility lies with the authors. Views expressed in the text are those of the authors and do not necessarily reflect the views of the publisher.

## Acknowledgements

The authors thank the Secretaria de Ciencia, Humanidades, Tecnologia e Innovacion (Ministry of Science, Humanities, Technology, and Innovation of Mexico; SECIHTI), and the professors, technicians, and students at the Department of Physical Oceanography of the Centre for Scientific Research and Higher Education of Ensenada.

## Financial support

This work was funded by a scholarship granted by Secretaria de Ciencia, Humanidades, Tecnologia e Innovacion (Ministry of Science, Humanities, Technology, and Innovation of Mexico; SECIHTI) under grant number CVU-1170291.

https://doi.org/10.5194/egusphere-2026-3754
Preprint. Discussion started: 2 July 2026


**Review statement**

The review statement will be added by Copernicus Publications listing the handling editor as well as all contributing referees according to their status anonymous or identified.

## References

Allende-Arandia, M. E., Duran, R., Sanvicente-Añorve, L., and Appendini, C. M.: Lagrangian characterization of surface transport from the Equatorial Atlantic to the Caribbean Sea using climatological Lagrangian coherent structures and self-organizing maps, J. Geophys. Res. Oceans, 128, e2023JC019894, https://doi.org/10.1029/2023JC019894, 2023.

Andrade-Canto, F., Beron-Vera, F. J., Goni, G. J., Karrasch, D., Olascoaga, M. J., and Triñanes, J.: Carriers of Sargassum and mechanism for coastal inundation in the Caribbean Sea, Phys. Fluids, 34(1), 016602, https://doi.org/10.1063/5.0079055, 2022.

Arellano-Verdejo, J., Lazcano-Hernandez, H. E., Prado Molina, J., Mendoza Castillo, U. D. J., Jiménez Escudero, V. M., Osorno Covarrubias, F. J., Gómez Rodríguez, G., Quintero Pérez, J. A., Czitrom Baus, S., Penié Rodriguez, I., and Tapia Varela, G.: Towards enhanced Sargassum monitoring in the Caribbean Sea, Sci. Rep., 15, 8965, https://doi.org/10.1038/s41598-025-93001-9, 2025.

Badan A., Jr., Candela, J., Sheinbaum, J., and Ochoa, J.: Upper-layer circulation in the approaches to Yucatan Channel, Geophys. Monogr. Ser., 161, 57–69, https://doi.org/10.1029/161GM05, 2005.

Berline, L., Ody, A., Jouanno, J., Chevalier, C., André, J. M., Thibaut, T., and Ménard, F.: Hindcasting the 2017 dispersal of Sargassum algae in the Tropical North Atlantic, Mar. Pollut. Bull., 158, 111431, https://doi.org/10.1016/j.marpolbul.2020.111431, 2020.

Beron-Vera, F. J., Olascoaga, M. J., and Goni, G. J.: Oceanic mesoscale eddies as revealed by Lagrangian coherent structures, Geophys. Res. Lett., 35, L12603, https://doi.org/10.1029/2008GL033957, 2008.

Beron-Vera, F. J., Olascoaga, M. J., Putman, N. F., Triñanes, J., Goni, G. J., and Lumpkin, R.: Dynamical geography and transition paths of Sargassum in the tropical Atlantic, AIP Adv., 12, 105107, https://doi.org/10.1063/5.0117623, 2022.

Bourg, N., Schaeffer, A., Cetina-Heredia, P., Lawes, J. C., and Lee, D.: Driving the blue fleet: Temporal variability and drivers behind bluebottle (Physalia physalis) beachings off Sydney, Australia, PLOS ONE, 17, e0265593, https://doi.org/10.1371/journal.pone.0265593, 2022.

Brooks, M. T., Coles, V. J., Hood, R. R., and Gower, J. F.: Factors controlling the seasonal distribution of pelagic sargassum, Mar. Ecol. Prog. Ser., 599, 1–18, https://doi.org/10.3354/meps12646, 2018.

Brooks, M. T., Coles, V. J., and Coles, W. C.: Inertia influences pelagic Sargassum advection and distribution, Geophys. Res. Lett., 46, 2610–2618, https://doi.org/10.1029/2018GL081489, 2019.

Candela, J., Sheinbaum, J., Ochoa, J., Badan, A., and Leben, R.: The potential vorticity flux through the Yucatan Channel and the Loop Current in the Gulf of Mexico, Geophys. Res. Lett., 29, 16–1, https://doi.org/10.1029/2002GL015587, 2002.

https://doi.org/10.5194/egusphere-2026-3754
Preprint. Discussion started: 2 July 2026


Caputi, N., Chubb, C., and Pearce, A.: Environmental effects on recruitment of the western rock lobster, Panulirus cygnus, Mar. Freshw. Res., 52, 1167–1174, https://doi.org/10.1071/MF01180, 2002.

Carrillo, L., Johns, E. M., Smith, R. H., Lamkin, J. T., and Largier, J. L.: Pathways and Hydrography in the Mesoamerican Barrier Reef System Part 1: Circulation, Contin. Shelf Res., 109, 164–176, https://doi.org/10.1016/j.csr.2015.09.014, 2015.

Centurioni, L. R. and Niiler, P. P.: On the surface currents of the Caribbean Sea, Geophys. Res. Lett., 30, 1279, https://doi.org/10.1029/2002GL016231, 2003.

Cetina, P., Candela, J., Sheinbaum, J., Ochoa, J., and Badan, A.: Circulation along the Mexican Caribbean coast, J. Geophys. Res. Oceans, 111, C08021, https://doi.org/10.1029/2005JC003056, 2006.

Cetina-Heredia, P., Roughan, M., Liggins, G., Coleman, M. A., and Jeffs, A.: Mesoscale circulation determines broad spatio-temporal settlement patterns of lobster, PLOS ONE, 14, e0211722, https://doi.org/10.1371/journal.pone.0211722, 2019.

Chavez, G., Candela, J., and Ochoa, J.: Subinertial flows and transports in Cozumel Channel, J. Geophys. Res. Oceans, 108, 3037, https://doi.org/10.1029/2002JC001456, 2003.

Chavez, V., Uribe-Martínez, A., Cuevas, E., Rodríguez-Martínez, R. E., van Tussenbroek, B. I., Francisco, V., Estévez, M., Celis, L. B., Monroy-Velázquez, L. V., Leal-Bautista, R., Álvarez-Filip, L., García-Sánchez, M., Masia, L., and Silva, R.: Massive Influx of Pelagic Sargassum spp. on the Coasts of the Mexican Caribbean 2014–2020: Challenges and Opportunities, Water, 12, 2908, https://doi.org/10.3390/w12102908, 2020.

Copernicus Marine Service: Global Ocean Physics Analysis and Forecast, Marine Data Store [data set], https://doi.org/10.48670/moi-00016, 2026.

Cuevas, E., Uribe-Martinez, A., and de los Angeles Liceaga-Correa, M.: A satellite remote-sensing multi-index approach to discriminate pelagic Sargassum in the waters of the Yucatan Peninsula, Mexico, Int. J. Remote Sens., 39, 3608–3627, https://doi.org/10.1080/01431161.2018.1447162, 2018.

Dagestad, K. F. and Röhrs, J.: Prediction of ocean surface trajectories using satellite derived vs. modeled ocean currents, Remote Sens. Env., 223, 130–142, https://doi.org/10.1016/j.rse.2019.01.001, 2019.

Dagestad, K. F., Röhrs, J., Breivik, Ø., and Ådlandsvik, B.: OpenDrift v1. 0: a generic framework for trajectory modelling, Geosci. Model Dev., 11, 1405–1420, https://doi.org/10.5194/gmd-11-1405-2018, 2018.

Ezer, T., Thattai, D. V., Kjerfve, B., and Heyman, W. D.: On the variability of the flow along the Meso-American Barrier Reef system: a numerical model study of the influence of the Caribbean current and eddies, Ocean Dyn., 55, 458–475, https://doi.org/10.1007/s10236-005-0033-2, 2005.

Fernandez-Partagas, J. and Mooers, C. N.: A subsynoptic study of winter cold fronts in Florida, Mon. Weather Rev., 103, 742–744, https://doi.org/10.1175/1520-0493(1975)103, 1975.

Haller, G.: Distinguished material surfaces and coherent structures in three-dimensional fluid flows, Phys. D, 149, 248–277, https://doi.org/10.1016/S0167-2789(00)00199-8, 2001.

Harrison, C. S. and Siegel, D. A.: The tattered curtain hypothesis revised: Coastal jets limit cross-shelf larval transport, Limnol. Oceanogr. Fluids Environ., 4, 50–66, https://doi.org/10.1215/21573689-2689820, 2014.

https://doi.org/10.5194/egusphere-2026-3754
Preprint. Discussion started: 2 July 2026


Hersbach, H., Bell, B., Berrisford, P., Biavati, G., Horányi, A., Muñoz Sabater, J., Nicolas, J., Peubey, C., Radu, R., Rozum, I., Schepers, D., Simmons, A., Soci, C., Dee, D., and Thépaut, J-N.: ERA5 hourly data on single levels from 1940 to present, Copernicus Climate Change Service (C3S) Climate Data Store (CDS) [data set], https://doi.org/10.24381/cds.adbb2d47, 2023.

Hu, C., Murch, B., Barnes, B., Wang, M., Marechal, J.P., Franks, J., Johnson, D., Lapointe, B., Goodwin, D., Schell, J., and Siuda, A.: Sargassum watch warns of incoming seaweed, Eos, 97, 10–15, https://doi.org/10.1029/2016eo058355, 2016.

Inoue, M., Handoh, I. C., and Bigg, G. R.: Bimodal distribution of tropical cyclogenesis in the Caribbean: Characteristics and environmental factors, J. Clim., 15, 2897–2905, https://doi.org/10.1175/1520-0442(2002)015, 2002.

Johns, E. M., Lumpkin, R., Putman, N. F., Smith, R. H., Muller-Karger, F. E., Rueda-Roa, D. T., Hu, C., Wang, M., Brooks, M. T., Gramer, L. J., and Werner, F. E.: The establishment of a pelagic Sargassum population in the tropical Atlantic: biological consequences of a basin-scale long distance dispersal event, Prog. Oceanogr., 182, 102269, https://doi.org/10.1016/j.pocean.2020.102269, 2020.

Johnson, D. R., Franks, J. S., Oxenford, H. A., and Cox, S. A. L.: Pelagic Sargassum prediction and marine connectivity in the tropical Atlantic, Gulf Caribb. Res., 31, GCFI20-GCFI30, https://doi.org/10.18785/gcr.3101.15, 2020.

Jouanno, J., Almar, R., Muller-Karger, F., Morvan, G., van Tussenbroek, B., Benshila, R., Marchesiello, P., and Kwasi Appeaning, A.: Socio-ecological vulnerability assessment to Sargassum arrivals, Sci. Rep., 15, 9998, https://doi.org/10.1038/s41598-025-94475-3, 2025.

Jouanno, J., Benshila, R., Berline, L., Soulié, A., Radenac, M. H., Morvan, G., Diaz, F., Sheinbaum, J., Chevalier, C., Thibaut, T., Changeux, T., Menard, F., Berthet, S., Aumont, O., Ethé, C., Nabat, P., and Mallet, M.: A NEMO-based model of Sargassum distribution in the tropical Atlantic: description of the model and sensitivity analysis (NEMO-Sarg1.0), Geosci. Model Dev., 14, 4069–4086, https://doi.org/10.5194/gmd-14-4069-2021, 2021.

Jouanno, J., Morvan, G., Berline, L., Benshila, R., Aumont, O., Sheinbaum, J., and Ménard, F.: Skillful seasonal forecast of Sargassum proliferation in the Tropical Atlantic, Geophys. Res. Lett., 50, e2023GL105545, https://doi.org/10.1029/2023GL105545, 2023.

Jouanno, J., Sheinbaum, J., Barnier, B., Molines, J. M., Debreu, L., and Lemarié, F.: The mesoscale variability in the Caribbean Sea. Part I: Simulations and characteristics with an embedded model, Ocean Model., 23, 82–101, https://doi.org/10.1016/j.ocemod.2008.04.002, 2008.

Lapointe, B. E.: Phosphorus-limited photosynthesis and growth of Sargassum natans and Sargassum fluitans (Phaeophyceae) in the western North Atlantic, Deep-Sea Res. A: Oceanogr. Res. Pap., 33, 391–399, https://doi.org/10.1016/0198-0149(86)90099-3, 1986.

Lapointe, B. E., West, L. E., Sutton, T. T., and Hu, C.: Ryther revisited: Nutrient excretions by fishes enhance productivity of pelagic Sargassum in the western North Atlantic Ocean, J. Exp. Mar. Biol. Ecol., 458, 46–56, https://doi.org/10.1016/j.jembe.2014.05.002, 2014.

https://doi.org/10.5194/egusphere-2026-3754
Preprint. Discussion started: 2 July 2026


Lara-Hernandez, J., Enriquez, C., Zavala-Hidalgo, J., Cuevas, E., van Tussenbroek, B., and Uribe-Martinez, A.: Sargassum transport towards Mexican Caribbean shores: Numerical modeling for research and forecasting, J. Mar. Syst., 241, 103923, https://doi.org/10.1016/j.jmarsys.2023.103923, 2024.

Large, W. G., McWilliams, J. C., and Doney, S. C.: Oceanic vertical mixing: A review and a model with a nonlocal boundary layer parameterization, Rev. Geophys., 32, 363–403, https://doi.org/10.1029/94RG01872, 1994.

Lévy, M., Ferrari, R., Franks, P. J., Martin, A. P., and Rivière, P.: Bringing physics to life at the submesoscale, Geophys. Res. Lett., 39, L14602, https://doi.org/10.1029/2012GL052756, 2012.

Liu, Y., and Weisberg, R. H.: Evaluation of trajectory modeling in different dynamic regions using normalized cumulative Lagrangian separation, J. Geophys. Res., 116, C09013, https://doi.org/10.1029/2010JC006837, 2011.

Lumpkin, R., and Centurioni, L.: Global Drifter Program quality-controlled 6-hour interpolated data from ocean surface drifting buoys, NOAA National Centers for Environmental Information [data set], https://doi.org/10.25921/7ntx-z961, 2019.

Marsh, R., Addo, K. A., Jayson-Quashigah, P. N., Oxenford, H. A., Maxam, A., Anderson, R., Skliris, N., Dash, J., and Tompkins, E. L.: Seasonal Predictions of Holopelagic Sargassum Across the Tropical Atlantic Accounting for Uncertainty in Drivers and Processes: The SARTRAC Ensemble Forecast System, Front. Mar. Sci., 8, 722524, https://doi.org/10.3389/fmars.2021.722524, 2021.

Marsh, R., Oxenford, H. A., Cox, S. A. L., Johnson, D. R., and Bellamy, J.: Forecasting seasonal sargassum events across the tropical Atlantic: overview and challenges, Front. Mar. Sci., 9, 914501, https://doi.org/10.3389/fmars.2022.914501, 2022.

Maurer, A. S., Neef, E. D., and Stapleton, S.: Sargassum accumulation may spell trouble for nesting sea turtles, Front. Ecol. Environ., 13, 394–395, https://doi.org/10.1890/1540-9295-13.7.394, 2015.

Moser, M. L. and Lee, D. S.: Foraging over Sargassum by western North Atlantic seabirds, Wilson J. of Ornithol, 124, 66–72, https://doi.org/10.1676/11-067.1, 2012.

Muñoz, E., Busalacchi, A. J., Nigam, S., and Ruiz-Barradas, A.: Winter and summer structure of the Caribbean low-level jet, J. Clim., 21, 1260–1276, https://doi.org/10.1175/2007JCLI1855.1, 2008.

Ochoa, J., Candela, J., Badan, A., and Sheinbaum, J.: Ageostrophic fluctuations in Cozumel channel, J. Geophys. Res. Oceans, 110, C02004, https://doi.org/10.1029/2004JC002408, 2005.

Ochoa, J., Sheinbaum, J., Badan, A., Candela, J., and Wilson, D.: Geostrophy via potential vorticity inversion in the Yucatan Channel, J. Mar. Res., 59, 725–747, https://doi.org/10.1357/002224001762674917, 2001.

Peng, Y., Xu, X., Shao, Q., Weng, H., Niu, H., Li, Z., Zhang, C., Li, P., Zhong, X., and Yang, J.: Applications of Finite-Time Lyapunov Exponent in detecting Lagrangian Coherent Structures for coastal ocean processes: a review, Front. Mar. Sci., 11, 1345260, https://doi.org/10.3389/fmars.2024.1345260, 2024.

Pérez-Santos, I., Schneider, W., Sobarzo, M., Montoya-Sánchez, R., Valle-Levinson, A., and Garcés-Vargas, J.: Surface wind variability and its implications for the Yucatan basin-Caribbean Sea dynamics, J. Geophys. Res. Oceans, 115, C10052, https://doi.org/10.1029/2010JC006292, 2010.

https://doi.org/10.5194/egusphere-2026-3754
Preprint. Discussion started: 2 July 2026


Podlejski, W., Berline, L., Nerini, D., Doglioli, A., and Lett, C.: A new Sargassum drift model derived from features tracking in MODIS images, Mar. Pollut. Bull., 188, 114629, https://doi.org/10.1016/j.marpolbul.2023.114629, 2023.

Putman, N. F., Beyea, R. T., Iporac, L. A. R., Trinanes, J., Ackerman, E. G., Olascoaga, M. J., Appendini, C. M., Arriaga, J., Collado-Vides, L., Lumpkin, R., and Hu, C.: Improving satellite monitoring of coastal inundations of pelagic Sargassum algae with wind and citizen science data, Aquat. Bot., 188, 103672, https://doi.org/10.1016/j.aquabot.2023.103672, 2023.

Putman, N. F., Goni, G. J., Gramer, L. J., Hu, C., Johns, E. M., Trinanes, J., and Wang, M.: Simulating transport pathways of pelagic Sargassum from the Equatorial Atlantic into the Caribbean Sea, Prog. Oceanogr., 165, 205–214, https://doi.org/10.1016/j.pocean.2018.06.009, 2018.

Putman, N. F., Lumpkin, R., Olascoaga, M. J., Trinanes, J., and Goni, G. J.: Improving transport predictions of pelagic Sargassum, J. Exp. Mar. Biol. Ecol., 529, 151398, https://doi.org/10.1016/j.jembe.2020.151398, 2020.

Richardson, P. L.: Caribbean Current and eddies as observed by surface drifters, Deep Sea Res. Part II, 52, 429–463, https://doi.org/10.1016/j.dsr2.2004.11.001, 2005.

Resiere, D., Kallel, H., Florentin, J., Banydeen, R., Compton, K., Gueye, P., Mehdaoui, H., and Neviere, R.: Sargassum seaweed in the Caribbean: A major public health problem still unsolved, J. Glob. Health, 13, 03017, https://doi.org/10.7189/jogh.13.03017, 2023.

Rodriguez-Martinez, R. E., Jordan-Dahlgren, E., and Hu, C.: Spatio-temporal variability of pelagic Sargassum landings on the northern Mexican Caribbean, Remote Sens. Appl. Soc. Environ., 27, 100767, https://doi.org/10.1016/j.rsase.2022.100767, 2022.

Rodriguez-Martinez, R. E., Medina-Valmaseda, A. E., Blanchon, P., Monroy-Velazquez, L. V., Almazan-Becerril, A., Delgado-Pech, B., Vasquez-Yeomans, L., Francisco, V., and Garcia-Rivas, M. C.: Faunal mortality associated with massive beaching and decomposition of pelagic Sargassum, Mar. Pollut. Bull., 146, 201–205, https://doi.org/10.1016/j.marpolbul.2019.06.015, 2019.

Rodriguez-Muñoz, R., Muñiz-Castillo, A. I., Euan-Avila, J. I., Hernandez-Nuñez, H., Valdes-Lozano, D. S., Colli-Dula, R. C., and Arias-Gonzalez, J. E.: Assessing temporal dynamics on pelagic Sargassum influx and its relationship with water quality parameters in the Mexican Caribbean, Reg. Stud. Mar. Sci., 48, 102005, https://doi.org/10.1016/j.rsma.2021.102005, 2021.

Rooker, J. R., Turner, J. P., and Holt, S. A.: Trophic ecology of Sargassum-associated fishes in the Gulf of Mexico determined from stable isotopes and fatty acids, Mar. Ecol. Prog. Ser., 313, 249–259, https://doi.org/10.3354/meps313249, 2006.

Roughan, M., Cetina-Heredia, P., Ribbat, N., and Suthers, I. M.: Shelf Transport Pathways Adjacent to the East Australian Current Reveal Sources of Productivity for Coastal Reefs, Front. Mar. Sci., 8, 789687, https://doi.org/10.3389/fmars.2021.789687, 2022.

Schell, J. M., Goodwin, D. S., and Siuda, A. N.: Recent sargassum inundation events in the Caribbean: Shipboard observations reveal dominance of a previously rare form, Oceanogr., 28, 8–11, https://doi.org/10.5670/oceanog.2015.70, 2015.

https://doi.org/10.5194/egusphere-2026-3754
Preprint. Discussion started: 2 July 2026


Shchepetkin, A. F. and McWilliams, J. C.: The regional oceanic modeling system (ROMS): a split-explicit, free-surface, topography-following-coordinate oceanic model. Ocean Model., 9, 347–404, https://doi.org/10.1016/j.ocemod.2004.08.002, 2005.

Shchepetkin, A. F. and McWilliams, J. C.: Correction and commentary for "Ocean forecasting in terrain-following coordinates: Formulation and skill assessment of the regional ocean modeling system" by Haidvogel et al., J. Comp. Phys. 227, pp. 3595–3624, J. Comp. Phys., 228, 8985–9000, https://doi.org/10.1016/j.jcp.2009.09.002, 2009.

Sheinbaum, J., Candela, J., Badan, A., and Ochoa, J.: Flow structure and transport in the Yucatan Channel, Geophys. Res. Lett., 29, 10-1–10-4, https://doi.org/10.1029/2001GL013990, 2002.

Skliris, N., Marsh, R., Addo, K. A., and Oxenford, H.: Physical drivers of pelagic sargassum bloom interannual variability in the Central West Atlantic over 2010–2020, Ocean Dyn., 72, 383–404, https://doi.org/10.1007/s10236-022-01511-1, 2022.

Sosa-Gutierrez, R., Jouanno, J., and Berline, L.: Sargassum spp. accumulation and transport by mesoscale eddies, Ocean Sci., 21, 1505–1514, https://doi.org/10.5194/os-21-1505-2025, 2025.

Uribe-Martinez, A., Berriel-Bueno, D., Chavez, V., Cuevas, E., Almeida, K. L., Fontes, J. V., van Tussenbroek, B. I., Mariño-Tapia, I., de los Angeles Liceaga-Correa, M., Ojeda, E., Castañeda-Ramirez, D. G., and Silva, R.: Multiscale distribution patterns of pelagic rafts of sargasso (Sargassum spp.) in the Mexican Caribbean (2014–2020), Front. Mar. Sci., 9, 920339, https://doi.org/10.3389/fmars.2022.920339, 2022.

van Sebille, E., Zettler, E., Wienders, N., Amaral-Zettler, L., Elipot, S., and Lumpkin, R.: Dispersion of Surface Drifters in the Tropical Atlantic, Front. Mar. Sci., 7, 607426, https://doi.org/10.3389/fmars.2020.607426, 2021.

van Tussenbroek, B. I., Arana, H. A. H., Rodriguez-Martinez, R. E., Espinoza-Avalos, J., Canizales-Flores, H. M., Gonzalez-Godoy, C. E., Barba-Santos, M. G., Vega-Zepeda, A., and Collado-Vides, L.: Severe impacts of brown tides caused by Sargassum spp. on near-shore Caribbean seagrass communities, Mar. Pollut. Bull., 122, 272–281, https://doi.org/10.1016/j.marpolbul.2017.06.057, 2017.

Wang, M., Hu, C., Barnes, B. B., Mitchum, G., Lapointe, B., and Montoya, J. P.: The great Atlantic Sargassum belt, Science, 364, 83–87, https://doi.org/10.1126/science.aaw7912, 2019.

Witherington, B., Hirama, S., and Hardy, R.: Young sea turtles of the pelagic Sargassum-dominated drift community: Habitat use, population density, and threats, Mar. Ecol. Prog. Ser., 463, 1–22, https://doi.org/10.3354/meps09970, 2012.

Zhong, Y. and Bracco, A.: Submesoscale impacts on horizontal and vertical transport in the Gulf of Mexico, J. Geophys. Res. Oceans, 118, 5651–5668, https://doi.org/10.1002/jgrc.20402, 2013.